



Sequential plug formation, disintegration by Vulcanian explosions, and the generation of granular Pyroclastic Density Currents at Tungurahua volcano (2013–2014), Ecuador



Minard L. Hall ^{*}, Alexander L. Steele, Benjamin Bernard, Patricia A. Mothes, Silvia X. Vallejo, Guilhem A. Douillet, Patricio A. Ramón, Santiago X. Aguaiza, Mario C. Ruiz

Instituto Geofísico, Escuela Politécnica Nacional, Ecuador

ARTICLE INFO

Article history:

Received 2 April 2015

Accepted 2 September 2015

Available online 10 September 2015

Keywords:

Plug formation

Cyclic Vulcanian explosions

Highest energy

PDC formation

ABSTRACT

Following 84 years of repose, Tungurahua volcano, Ecuador initiated its present eruptive episode in October 1999, but its PDC activity only began in July 2006. A period of highly energetic Vulcanian eruptions started in 2012, those of 14 July 2013, 18 October 2013, and 1 February 2014 being the most important. These eruptions were well-monitored by a 5-station broadband seismic and acoustic array. Repeated repose intervals of ~3.5 months between Vulcanian events (VEI ~2) suggest that gases in the ascending juvenile magma experienced sequential pressurization cycles, as magma of preceding eruptive events solidified to form plugs that sealed the conduit. Every 34 months plug failure occurred, abrupt decompression followed, and the resulting Vulcanian explosions are associated with the highest seismic and acoustic energies ever registered anywhere. Small to moderate-sized PDC flows associated with the explosions and fountain collapses were generated and traveled ≤7 km down the steep N, NW, and W flanks of Tungurahua's cone at velocities of 11 to 18 m/s, although a small lateral blast and its PDC were clocked at 33 m/s descending the N flank. The explosive fragmentation of the plugs (a dense microcrystalline andesite) and the juvenile magma (a vesiculated glassy andesite) comprise the principal rock fragments of the PDC deposits. Each deposit typically consisting of two layers; a thin upper layer of large segregated and abraded clasts with few fines and a thicker lower layer that is fines-rich with few large clasts. Many deposits were studied and photographed within a few days of their formation, which are presented.

© 2015 Elsevier B.V. All rights reserved.

1. Introduction

Pyroclastic Density Currents (PDCs) often accompany volcanic eruptions and because of the danger they represent they have been given considerable attention. Ash flows and other matrix-rich pyroclastic flows have been studied in notable detail ever since the 1912 Katmai eruption (Williams, 1941; Hildreth and Fierstein, 2012). Less attention has been given to granular PDCs (Freundt et al., 2000; Iverson and Vallance, 2001) because of the poor understanding of the state of fluidity and the transport mechanisms of such flows. Wilson and Head (1981) called attention to this lack of understanding in their extensive list of PDC phenomena that require better descriptions and explanations, which is the aim of this report.

The detailed observations of the eruptions and deposits of the 1995–1999 Soufriere Hills Volcano, Montserrat (Cole et al., 2002; Drituit et al., 2002; Loughlin et al., 2002; Ritchie et al., 2002, among others) contributed greatly to our knowledge and perceptions about the formation of

granular PDCs, especially in a growing dome scenario. Multidisciplinary studies of the 2010 Merapi eruption (Charbonnier et al., 2013; Cronin et al., 2013; Jenkins et al., 2013; Komorowski et al., 2013) provided further insights into dome-generated granular PDCs and their emplacement.

Tungurahua volcano, Ecuador (5020 masl) became active in late 1999, following an 84-year pause, however no PDCs were generated until July and August 2006 (Kelfoun et al., 2009; Douillet et al., 2013; Hall et al., 2013; Bernard et al., 2014). From 2007 to 2013 at least 5 eruptive phases produced PDCs (March 2007, February 2008, May and December 2010, December 2012). In mid-2013 and continuing into mid-2014, a cycle of large Vulcanian explosions began, associated with inferred plug formation and destruction, and often accompanied by PDCs.

This report is of general interest because (1) Tungurahua's PDCs were generated by abrupt, very energetic Vulcanian explosions through conduit plugs that resulted in only moderate-sized eruptions; (2) their occurrence was closely monitored by seismic, infra-sound, and acoustic flow monitors, as well as by photographic, video, and thermal imagery; and (3) the resulting PDC deposits were studied almost immediately, before they could be eroded or modified. This study is useful for

^{*} Corresponding author.

comparing plug-generated PDC events and their deposits with those of dome origin.

2. Eruption onsets – seismic and acoustic signals

The PDC events documented here correspond to the 14 July and 18 October eruptions of 2013 as well as to the 1 February 2014 event. Henceforth, these three eruptions will be referred to as the 14 July, 18 Oct, and 1 Feb events. Their initial explosions generated small to medium-sized PDC flows of the block-and-ash type that could be visited and studied conveniently. These eruptions were monitored by a 5-station broadband seismic and infrasound network, as well as by acoustic flow monitoring (AFM) stations, all telemetered in real time to the Instituto Geofísico's nearby observatory (OVT). Descriptions and location of this network were given in Hall et al. (2013). Here, it is relevant to briefly indicate the intensities of the three explosions discussed in this paper, determined from recorded seismic and acoustic (infrasound) data. All three events were Vulcanian in nature with abrupt onsets and high energies, suggesting that the volcano's conduit had been tightly plugged. Furthermore, the crater's shape has suffered little modification during these eruptions, suggesting that the Vulcanian explosions were not shallow in origin, possibly as deep as ~1.5 km, as noted by Kim et al. (2014).

The three explosion sequences (EX1–3) are all representative of discrete Vulcanian outbursts that were associated with PDC events (Table 1). All three display seismic waveforms characterized by low frequency signals, emergent compressional onsets and long codas. In contrast, the acoustic signals are represented by impulsive compressional onsets followed by strong rarefaction pulses that form the typical 'N-shaped' acoustic waveform characteristic of Vulcanian explosions (Morrissey and Chouet, 1997; Petersen et al., 2006; Johnson and Ripepe, 2011; Fee and Matoza, 2013). Furthermore, the waveform structure, the intensities and energies of the eruptions and the visual observations of the events support the interpretation that all three explosions were accompanied by a shockwave component.

EX1 of 14 July 2013 registered seismo-acoustic amplitude and energy levels larger than any other discrete explosion event at Tungurahua since up-graded monitoring began in July 2006. EX1 was the first event of this eruptive episode and is considered the vent-opening pulse that was immediately followed by continuous tremor, interpreted to be the ascent of explosion debris in the conduit as well as the column of volcanic material that ultimately extended to an altitude of ~8.3 km above the crater floor (4800 m elevation). A series of pyroclastic flows followed. EX1 was heard by inhabitants over 180 km away.

In terms of seismic energy radiated, an averaged (E_S _MEAN) value for the EX1 explosion was calculated at $\sim 1.9 \times 10^9$ J, approximately 14% larger than any other explosion at Tungurahua during the last seven and a half years of monitoring, while an extraordinary acoustic energy radiated into the atmosphere generated a far-field estimate of

$\sim 3.2 \times 10^{11}$ J, a value about two and a half times larger than any other discrete explosion recorded at the volcano since 2006. Acoustic energy for EX1 was found to be approximately two orders of magnitude larger than seismic energy, a trend in energy partitioning consistent with discrete explosive sequences at Tungurahua.

Petersen et al. (2006) note that acoustic energy radiated from large Vulcanian explosions at Augustine volcano (Alaska) in January 2006 reached $\sim 4 \times 10^9$ J, a value of acoustic energy two orders of magnitude lower than that of EX1. Acoustic explosion energy at Tungurahua also exceeded estimates of Strombolian explosions at Erebus and Karymsky volcanoes (max. $\sim 2 \times 10^7$ J; Johnson and Aster, 2005) and from explosions at Villarrica and Fuego volcanoes (max. $\sim 7.6 \times 10^4$ J and 2.2×10^7 J, respectively; Marchetti et al., 2009). Seismic amplitudes from the January 2006 eruptions at Augustine had values up to 178 cm^2 (McNutt et al., 2010), considerably lower than seismic reduced displacement values approximated for EX1 (616 cm^2).

Although EX2 and EX3 also display high amplitude and energy approximations, these events are considered to be in the medium-to-large range for explosions at Tungurahua, when based on amplitude and energy estimates from over 5500 discrete explosive sequences recorded between July 2006 and February 2014. During this seven and a half year monitoring period, PDC activity has been rare, observed on fewer than 50 individual days and not necessarily triggered by the most intense Vulcanian eruptions. Indeed, we find that no correlation exists between the magnitude or intensity of the explosions and the prospect of PDC activity.

Since 2010, Tungurahua's eruptive episodes have become shorter in duration, but more intense and with higher energy explosions. From 21 August 2012 to 1 February 2014, repose intervals between Vulcanian eruptions were 3.5, 7, 3, and 3.5 months long. This periodicity suggests that the magma experienced sequential pressurization cycles in the conduit behind consecutive, but discrete magmatic plugs. Furthermore, the increased frequency of high-energy Vulcanian-style explosions since 2010 (as highlighted by EX1–3) strongly supports the inference that the formation of solidified plugs in the conduit may have played an important role in the recent explosive activity.

3. PDC paths

The 14 July and 1 Feb explosions generated PDCs that followed drainages on the N, NW, W, and SW flanks of Tungurahua's cone (Fig. 1), similar to those of the 2006 PDCs but to a lesser extent (Kelfoun et al., 2009; Hall et al., 2013; OVT Weekly Reports). The 18 Oct PDC, being of small volume, descended directly down the NW flank and ended near the 2900 m contour.

The 1 Feb PDC onset was captured by video whose images are consistent with three types of PDC genesis: a low-level fountain collapse, a slightly higher fall-back from the eruption plume, and that of a high

Table 1
Amplitudes and energies of explosions associated with PDC events.

Explosion no. (EX)	Date & time (UTC)					D_R _MEAN (cm^2)	P_R _MEAN (Pa)	E_S _MEAN (J)	E_A _MEAN (J)	Plume height (km)
	YY	MM	DD	HH	mm					
EX1	2013	07	14	11	46	616	5327	$1.93\text{E} + 09$	$3.20\text{E} + 11$	8.3
EX2	2013	10	18	14	26	137	3056	$1.91\text{E} + 08$	$2.60\text{E} + 10$	4.1
EX3	2014	02	01	22	39	197	1823	$2.05\text{E} + 08$	$3.40\text{E} + 10$	8.8

1. EX: explosion number.

2. YY: year; MM: month; DD: day; HH: hour; mm: minute. All times given are UTC.

3. D_R _MEAN: seismic reduced displacement (cm^2). Values corrected to source (vent).

4. P_R _MEAN: acoustic reduced pressure (Pa). Values corrected to 1 km from source (vent).

5. E_S _MEAN: seismic energy (J).

6. E_A _MEAN: acoustic energy (J).

7. Plume height above crater (km). (Source: VAAC, Washington D.C.)

*_MEAN: mean values are calculated from four stations (BMAS, BPAT, BRUN, and BBIL), each comprising a collocated seismic broadband instrument and an acoustic sensor. Details are presented in the accompanying Appendix A.

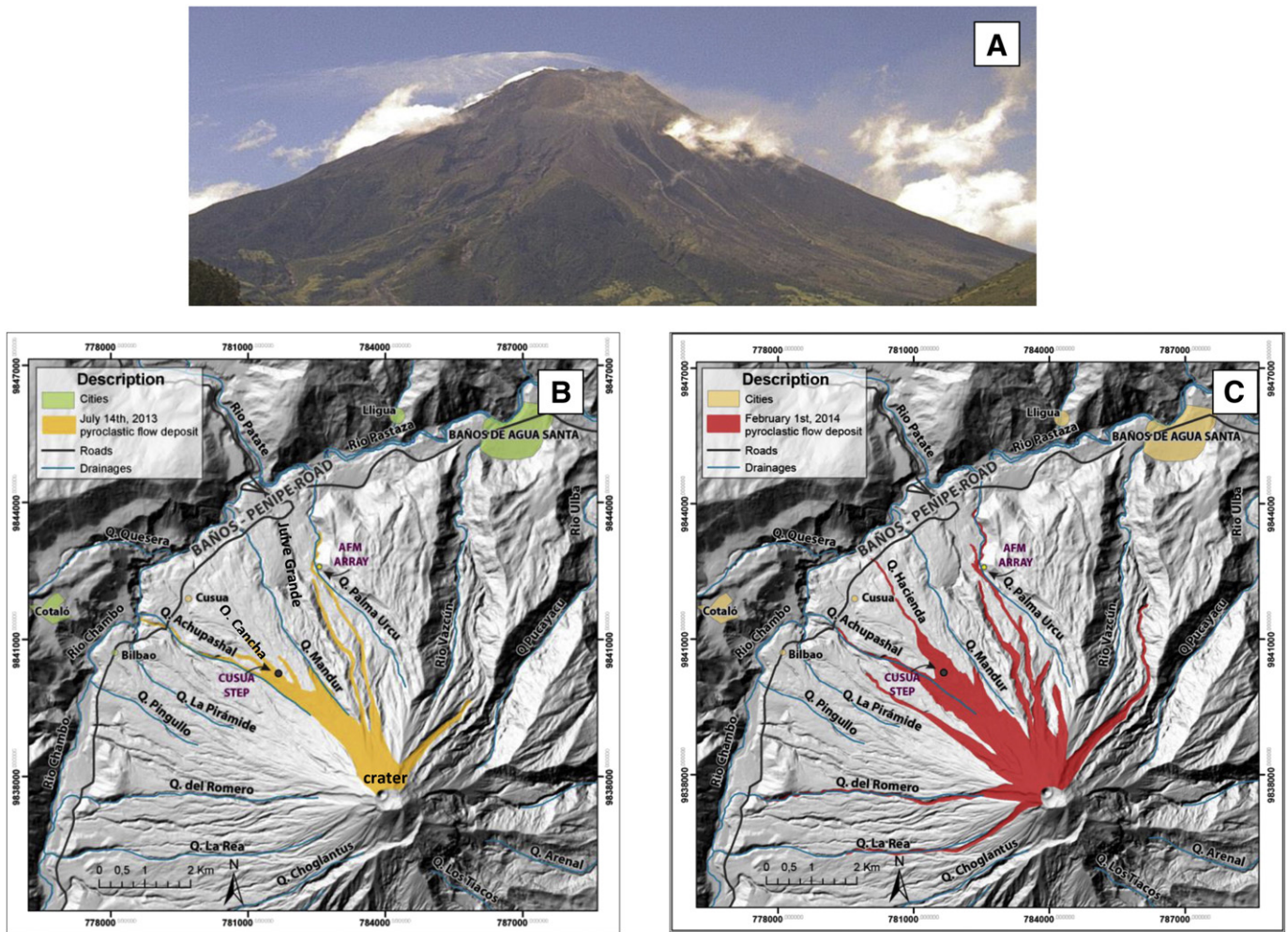


Fig. 1. A – West flank of Tungurahua volcano (5020 m). Width of view ~5 km. B – PDC routes of 14 July 2013 eruption. C – PDC routes of 1 February 2014 eruption.

velocity directed blast. The main PDCs were initiated by fountain collapse that fell upon the upper NW flank.

The PDCs of the 14 July and 1 Feb eruptions descended two principal drainages, comprised of tributaries of the Juive Grande–Palma Urco (JG–PU) and the Achupashal (A) valleys. PDCs also descended smaller ravines including those of the Rea, Romero, Cancha, Hacienda, Mandur, and Vascún drainages (Fig. 1). More specifically, the 14 July PDCs descended the Achupashal, Cancha, Mandur, the JG–PU ravines, and the Vascún valley (Fig. 1B). The 1 Feb PDCs followed the Rea, Romero, Achupashal (both N and S forks), Hacienda, Mandur, and the two main JG–PU channels, as well as the Vascún valley, stopping only 3 km above Baños, the main city in the area with $\geq 20,000$ inhabitants (Fig. 1C). The following description is based chiefly upon field and aerial observations and topographic profiles. Slope distances are employed here.

The Achupashal ravine is 7.5 km long and reaches the Chambo river at 2060 masl. It descends the NW flank of the cone from the low spot on the crater rim at 4835 m. Both the 14 July and 1 Feb PDCs traveled down the smooth, inclined upper slope (average 28° ; range $35\text{--}15^\circ$) of the cone for a distance of 3.4 km until they reached the Cusua Step, a 1 km-long lesser-inclined topographic step. They then entered the Achupashal ravine, a deeply-incised ravine, 30–40 m wide, which has a series of vertical drops with an overall gradient of 17° (range $20\text{--}10^\circ$) until it joins the Chambo river. The total slope distances traveled by the 14 July and 1 Feb PDCs along the Achupashal route are 7.5 and 6.8 km, respectively.

The Juive Grande–Palma Urco route is 8.2 km long and reaches the Pastaza river at 1850 masl. Its PDCs began at the same low spot on the crater's rim and descended NNW-ward down an evenly-inclined upper slope (ave. 30° ; range $35\text{--}25^\circ$) for 1.6 km. Then the 14 July and 1 Feb PDCs entered a 20–40 m wide stepped ravine of the upper Juive drainage for about 2.4 km that included a series of steep to vertical drops of 5–15 m with an overall gradient of 26° (range $30\text{--}20^\circ$). Subsequently these PDCs reached the lower Juive path, a 1.8 km-long trough with an average slope of 18° (range $20\text{--}15^\circ$), where some flows terminated. At the trough's end near the AFM array (Fig. 1C), most of the PDCs turned to the right and entered the lower Palma Urco ravine, 20–30 m wide and 20–30 m deep, with an average gradient of 11° (range $15\text{--}10^\circ$). In this ravine both PDCs stopped about 500 m above the Baños–Pelileo highway, a key highway that connects the Andes to the Amazon Basin. The total slope distances traveled by both the 14 July and 1 Feb PDCs along the JG–PU route are ~7.3–7.4 km, corresponding to a total vertical drop of 2.8 km.

In general these ravines are dry and only briefly carry water after important rainfalls. No vegetation exists along the bottom of these ravines. The PDCs described herein flowed almost exclusively upon eroded lavas or older PDC and lahar rubble, especially at the lower elevations.

4. Rock types

Four principal rock types, all andesites, dominate the PDC deposits discussed here. Tungurahua's andesitic magmas have been relatively

uniform in their chemical compositions (58–59% SiO₂) during the past centuries (Hall et al., 1999; Le Pennec et al., 2008; Samaniego et al., 2011). In addition, Samaniego et al. (2011) concluded that Tungurahua's 2006 PDCs were the result of a mafic magma intrusion into an andesitic reservoir, followed by mixing and pressurization of the chamber.

(1) A rock type common to both the 14 July and 1 Feb PDC deposits is a black vesiculated andesite (1.5–1.6 g/cm³) with a glassy to microcrystalline matrix that carries few micro-phenocrysts of plagioclase ($\leq 10\%$) and fewer pyroxenes and olivine. These andesites have up to 50% vesicles, the remainder being principally an intra-bubble glassy matrix (Fig. 2A). Two ranges of bubble-size are noted: 3–10% are bubbles of

5–10 mm diameter and the remainder are small 1–3 mm bubbles. Most bubbles are spherical in shape. One variety of this rock type is the chilled-margin breadcrust clasts that are occasionally found in the 1 Feb PDC deposits. They have dark gray to black glassy perimeters and black vesiculated interiors with micro- to small (≤ 2 mm) vesicles.

That this rock type is the principal juvenile rock is implied by its presence as pristine bombs (Fig. 2B) and its occurrence as solidified foam in expansion cracks within blocks of the dense plug rock; its likely source was the de-gassing juvenile magma that ascended following decompression. Wright et al. (2012) concluded that low crystallinity in recent glass-rich rocks of Tungurahua suggests high rates of magma decompression as well as high ascent rates for the magma.

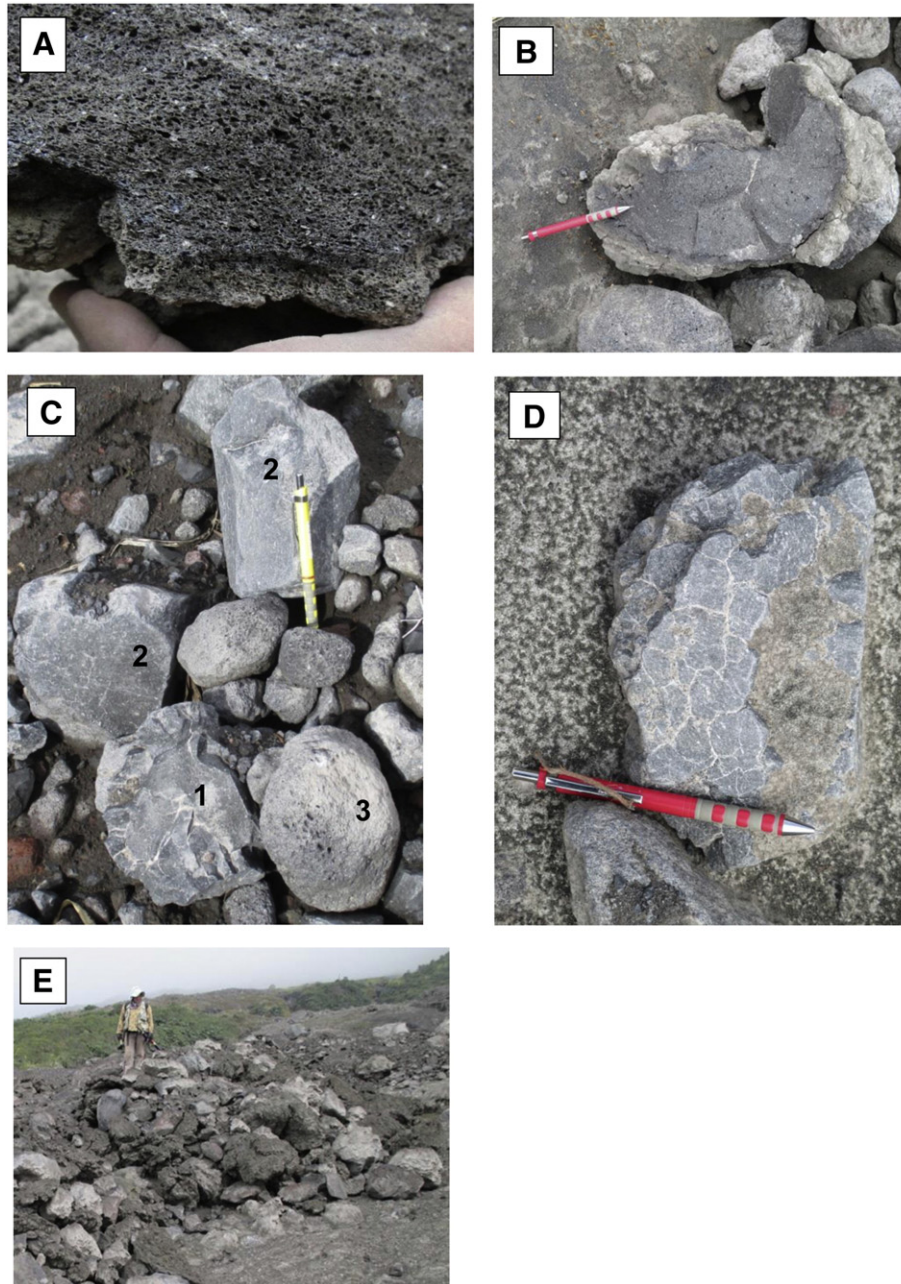


Fig. 2. Dominant rock types of the 2013 and 2014 PDC deposits, all of which are andesites of ~58% SiO₂. A – Well-vesiculated black andesite with very small plagioclase and pyroxene crystals thought to be the juvenile material (14 July PDC; Achupashal). B – Juvenile micro-vesicular andesite bomb with quenched rind found in the top layer of the 14 July PDC deposit at Achupashal. C – Frequently observed dense non-vesicular micro-crystalline (m-xl) andesites of the presumed plug seen in the 1 Feb PDC deposit of lower JG ravine. Rock 1 = the presence of this m-xl clast implies that ejected plug fragments were sufficiently hot to form chilled perimeters during the explosion. Rock 2 = typical sub-angular dense m-xl clasts. Rock 3 = rounded, abraded vesicular juvenile andesitic clast from the PDC's top layer. D – Non-vesicular dense andesite with numerous random micro-fissures with white salt infillings and chilled rind (1 Feb PDC; lower JG ravine). E – Reddish-brown cauliflower-head scoria blocks and whitish dense angular andesite blocks frequently observed in the 14 July PDC deposits (top of Hacienda ravine).

(2) The most common rock is the gray to dark gray dense (~2.6–2.7 g/cm³) non-vesicular andesite with a glassy-appearing exterior, that is however microcrystalline in thin-section (E. Gaunt, pers. comm., 2015). They commonly occur as large meter-sized blocks that have smooth faceted sides and expansion cracks. Many clasts have 1–2 cm thick chilled perimeters (Fig. 2C), implying that the rock was solid, hot, and mainly de-gassed at the time of the eruption. Furthermore, some clasts of the 1 Feb deposits have perimeters comprised of numerous shallow micro-fissures of random orientation, whose appearance suggests a mesh net with 1–2 cm-wide openings (Fig. 2D). Many of these micro-fissures contain white salts often attributed elsewhere to condensed magmatic gases, sometimes reported in dome rocks. If so, it would imply that these fissures formed during cooling of these rocks near the top of the conduit prior to fragmentation. The rock's abundance and degassed character strongly suggest that they were plug rocks of the conduit, most likely the solidified magma of preceding eruptive episodes. They are not considered to be dome rocks, as domes have never been observed in any recent cycle. Wright et al. (2007) thought that dense aphanitic andesites with thin rinds might reflect low water contents and poor bubble formation of the magma, as was argued by Samaniego et al. (2011) for Tungurahua's 2006 magmas.

(3) Cauliflower-head scoria clasts are more readily seen in the 14 July PDC deposits where they are generally 10 to 100 cm in size, reddish-brown in color, and comprise 10–20% of all clasts (Fig. 2E). They are similar to the so-called molten clots common in the 16 August 2006 PDC deposits (Douillet et al., 2013; Hall et al., 2013), which were notable for having molten features around their entire perimeter, suggesting that they solidified in air. The clast's interior is similar in appearance to the black vesiculated andesite described above; they are also rich with gas bubbles and have densities of 1.5–1.6 g/cm³. They are less common in the 1 Feb deposits and were not observed in the 18 Oct deposits. These scoria clasts are thought to represent the gas-rich top of the ascending magma column that presumably exited immediately after the plug's explosive fragmentation.

(4) The fourth rock type is composed of accidental rock fragments belonging to past eruptions that were apparently incorporated by the explosion from conduit walls or by the passage of the PDCs down the ravines. Scarlet-red scoria blocks, gray andesite clasts of different textures, and brown andesite clasts belong to this group. These are more abundant in the 14 July PDC deposits, comprising 5–15% of the total clast population.

5. PDC deposits: morphology and contents

Thermal imagery of the eruption shows that on the upper steep flanks of the cone, the fallback material formed incandescent blankets of coarse debris, whose downslope distribution was controlled by the steepness of the cone and small gullies. Most PDCs however began as dark billowing clouds that came from the summit area and descended the slopes with notable speed. Toward the intermediate elevations (3000–4000 masl), the PDCs began forming clast-rich streams that filled the ravines or spread out over more gradual slopes or upon topographic steps to form thin lobate deposits, 10–30 m wide.

The ravines have widths of 20–40 m, depths of 10–25 m, and gradients of 14–17°. In many cases the PDC deposits were voluminous enough to fill the ravine with planar wall-to-wall deposits. In others, the granular PDCs traveled as pulses that left lobe-shaped deposits toward the center of the ravine. These have convex profiles in cross-section, clast-rich snouts and lateral margins, and no levees. Individual lobes are generally 3–10 m wide, 1–2 m thick, and are stacked one upon another. As seen in Fig. 3A, the JG–PU ravine was filled by a series of granular pulses in which the subsequent pulse was less energetic and unable to override or pass the preceding flow deposit. These deposits often have uniform thicknesses along their down-valley lengths, especially where the channel gradients are constant. Upstream within tens of meters, individual pulses become less discrete and blend into the

general granular deposit (Fig. 3A, B). The flow's top surface is composed of a layer, ≤1 m thick, of well-sorted larger clasts, 5–30 cm in size (Fig. 3B, C).

Where the PDCs descended more gradual slopes and were not constrained laterally, such as upon topographic steps or depositional fans, they tended to form wider lobate deposits with marginal levees. These PDC lobes are generally 10–40 m wide, up to 1–1.5 m thick, and have flat surfaces bounded by 25–50 cm high levees. Both the levees and the deposit's surface generally carry clasts 5–50 cm in diameter, but at times they reach several meters in size (Fig. 7C). Where lobes terminate, they tend to have slightly convex snouts and lateral margins of coarser clasts.

Typical block-and-ash PDC deposits, observed in both the 14 July and 1 Feb PDCs and along both the JG–PU and A ravines, consist of a thinner, clast-rich, fines-poor top layer and an underlying, thicker, fines-rich main layer (Fig. 3B, C, D). Their shared contact is transitional on a millimetric scale. No basal sole unit was discerned in any of these PDC deposits, the contact with older pre-existing beds being sharp. In the JG ravine the 14 July PDC deposit is ~5 m thick and inversely graded, while the overlying 1 Feb deposit is only 1–1.5 m thick and mainly non-graded (Fig. 3D). The inversely graded PDC deposits contrast notably with the normal graded deposits of the 1997 Soufrière Hills PDCs (Ritchie et al., 2002). A description of the 14 July and 1 Feb PDC deposits follows.

The upper layer of the 14 July PDC deposit in the lower JG–PU ravine is commonly 15–40 cm-thick, composed chiefly of sub- to well-rounded andesite clasts that typically measure 10–25 cm in diameter and are well-sorted. The dominant clast is the black well-vesiculated glassy andesite, often with incipient breadcrust-like perimeters (Fig. 3C). In addition, subordinate clasts of the gray dense non-vesicular andesite, only slightly rounded, are recognized, as well as a few multi-colored accidental blocks. Cauliflower-head scoria blocks are more often observed in small groups, where they appear to have been stranded together by obstacles along the flow path. In most cases the top layer's rocks are clast-supported and devoid of any intra-clast matrix (Figs. 3C, 7E).

The dominance of vesiculated andesite clasts in the upper layer and their near absence in the underlying main layer are consistent with the interpretation that their lighter density may have favored their upward segregation. This top layer has many of the segregation characteristics reported by Iverson and Vallance (2001) and Johnson et al. (2012) who observed that larger clasts often migrate upward as well as outward toward the top and margins of granular flows. The abundance of rounded and abraded clasts in the upper layer, while the main layer carries more angular clasts, implies that intra-clast abrasion was especially important in the top layer (Fig. 3C, E). The fragile nature of the glassy vesiculated andesite favored rounding by clast-to-clast abrasion, which in turn would likely produce significant amounts of very fine rock powder, such as observed in some Tungurahua ashes (Eychenne et al., 2011). The lateral margins and snouts of the top layer carry a higher percentage of large clasts (Figs. 3B, 4D), also reported by Douillet et al. (2013).

The clasts of the PDC's top layer appear to become smaller and more uniform in size with distance downstream. At a distance of 4.4 km from the crater, large blocks (1–6 m) accompany the typical 10–25 cm clast fraction (Fig. 7A, B), while at 5.9 km and 6.9 km down along the JG path, large blocks are few and the surface clasts are generally smaller (5–20 cm in diameter) (Figs. 3C, 7E). Infrequently, the clast-rich top layer is replaced or swamped by the matrix-rich core of the lobe which then becomes the surface deposit, as seen in the 1 Feb deposit (Fig. 8D). Where PDCs were accompanied by surge units, centimeter-thick ash layers cover its bouldery surface. In A ravine on the day of the 14 July eruption a co-PDC ashy layer formed an ~10 cm thick mantle upon its coarse deposit (Fig. 4A) that was hot, fluidized, and readily deflated by stomping on it.

The underlying poorly-sorted fines-rich main layer of the 14 July PDC is often several meters thick; it may be non-graded or clearly

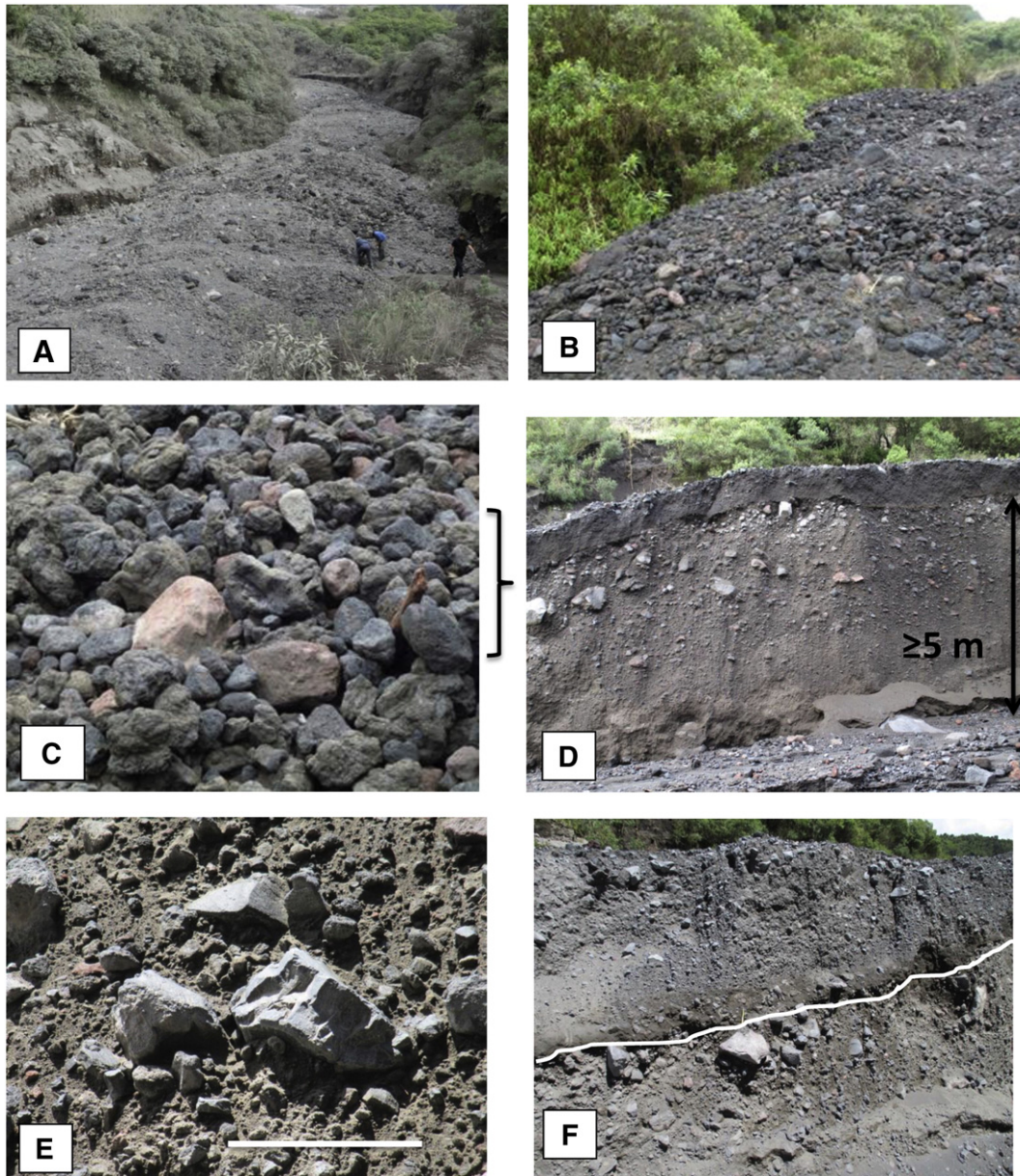


Fig. 3. The 14 July PDC in Juive Grande ravine, 6.6 km from the crater, 10 hours after its occurrence. A – The flow filled the ravine from side-to-side and has a convex cross-section. The flow advanced down valley from the back of the photo to the front. The flow's top surface is undulating, formed by a series of pulses, shingled one upon another as the series retreated. Note the people and roadway for scale. B – Close-up of (A) showing a lobe front with segregated rock clasts that form the lobe's top layer. Note the unaffected vegetation. The absence of PDC-surge deposits is due to surge having been decoupled and detoured up valley. Medium gray diamond-shaped rock in the lower right-corner is 50 cm across. C – Close-up of PDC's top layer composed of sub-rounded, abraded blocks in a clast-supported, matrix-free layer. Both juvenile and dense plug rocks are present. Other clasts are accidental blocks or scoria-head blocks. Large pink dome-shaped clast is ~20 cm across. D – Stream cut at the same location months later exposes the 5 m-thick 14 July PDC deposit overlain by the dark 1 m-thick 1 Feb PDC bed. Note the fines-rich interior and inverse grading of the 14 July PDC unit. Enclosure symbol in (C) shows the position of the clast-rich layer at the top of the 5 m-thick 14 July matrix-rich deposit. E – Close-up of the 14 July PDC matrix showing the dominance of angular clasts of the gray dense non-vesicular andesite, some with chilled rinds. White line is 8 cm long. F – Same outcrop as (D), showing the darker gray color and fewer clasts of the 1 Feb PDC deposit above the line and the 14 July PDC deposit below the line.

inversely-graded (Fig. 3D). The layer is typically rosy grayish-tan in color, moderately consolidated, and generally composed of $\geq 70\%$ silt- and sand-sized particles (generally ≤ 0.5 mm in size) (Fig. 3D, E). No micro-stratification or gas-escape pipes were observed. This unit carries sub-angular to angular clasts that range from a few centimeters to tens of centimeters in size. Gray dense andesite clasts, generally angular in shape, dominate, but small slightly rounded clasts of black vesicular andesite are also present (Fig. 3E). Cauliflower scoria clasts are not seen in this layer. Large rounded clasts are rarely observed in the main body, implying that block-to-block collisions were few or cushioned by the matrix.

The abundant fine-grained material was presumably derived from the inherent fragmentation of the solidified conduit rocks and ascending magma column during decompression and the Vulcanian onset, as well as from the collisions and abrasion of fragments during PDC descent. Stix et al. (1997) attributed the abundant fines of granular PDCs to the extreme disintegration of vesicle-rich magma produced by the decompression of highly pressurized conduits, a scenario similar to that presented here.

The abraded rounded clasts of the top layer are thought to originate by multi-collisions in a matrix-free or -poor continuum; conversely the fine-grain matrix of the main layer would likely diminish abrasion

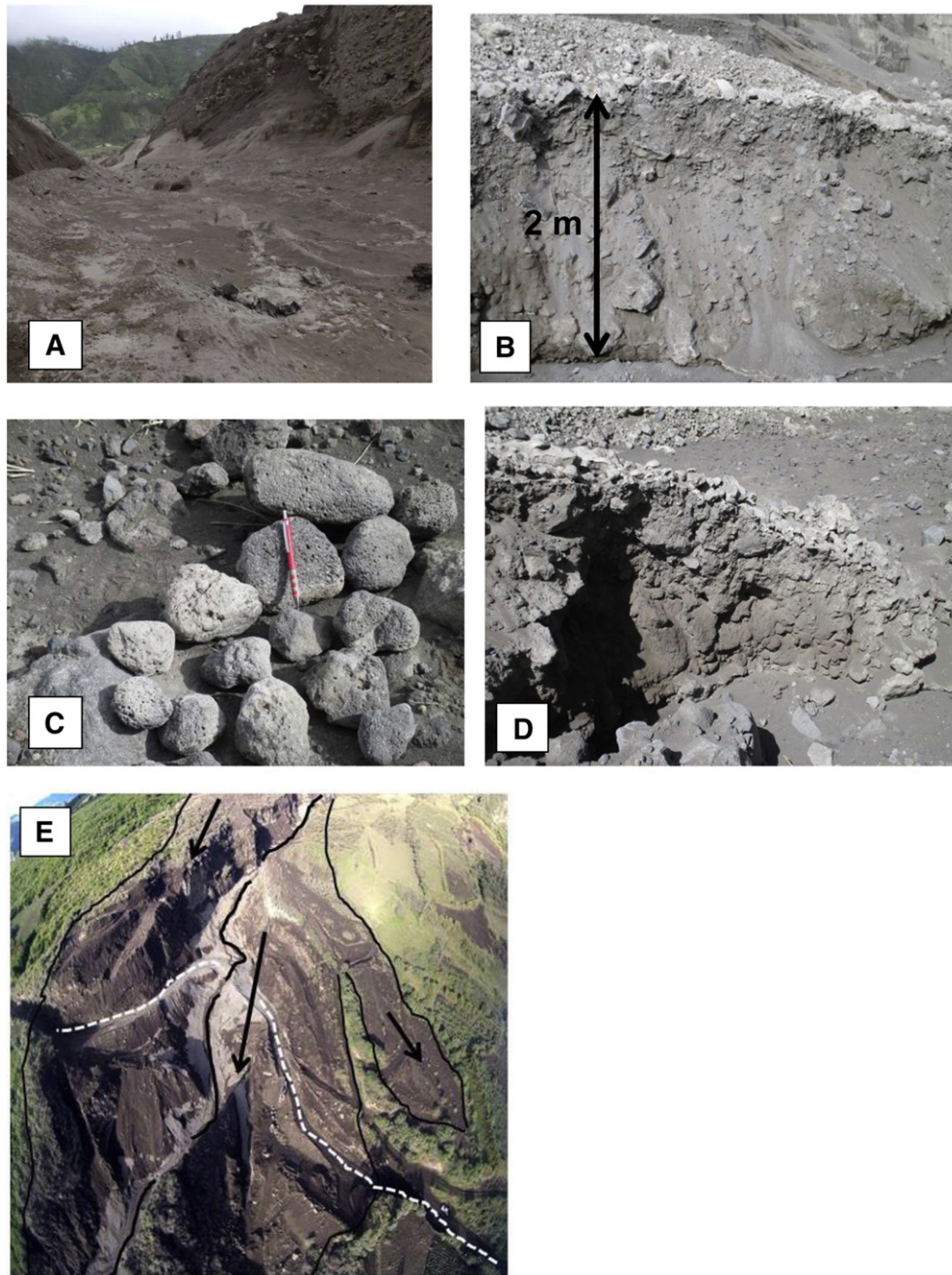


Fig. 4. The 14 July PDC deposits as observed on that day in the Achupashal ravine. A – The PDC deposit, covered with the gray ash of its PDC-surge, was confined to this narrow steep-sided valley. The surge's ash was hot, fluidized, and rapidly deflated by stomping. B – The PDC's block-and-ash interior is poorly sorted, ungraded, and unstratified. It has a matrix rich in both fines and clasts; most clasts tend to be angular, not rounded. The top layer is not well-segregated, containing both angular and rounded clasts. C – Examples of well-rounded, abraded clasts of the juvenile vesiculated andesite that often dominate the top layer. D – Cross-sectional view of the PDC lobe's snout seen in (B). Note the abundant angular clasts and diminutive quantity of fines. Apparently the flow segregated larger clasts by carrying them forward within the matrix, probably helping to brake the lobe's forward movement. E – Aerial view of A ravine and its intersection with the 10 m-wide Baños-Penipe road (white dashed line). Thick black line shows the ravine descending toward the lower left-side of the photo. Thin black lines show the limits of the 14 July PDC-surge on the adjacent hillsides. Photo by drone helicopter (J. Stone).

associated with clast collisions, and at the same time would likely have provided a medium that was partially fluidized by air entrainment during the 14 July PDC's descent. The notable co-PDC ash activity recorded by video imagery and the thin layer of fine ash that covered the PDC deposits is in agreement with this interpretation.

The 18 Oct PDC deposits were observed where its flows terminated on the Cusua Step. Its distribution and character were not studied, as most deposits occur in the higher restricted slopes of the volcano. Near its termination, its PDC deposit is small, ~5 m wide, and 30 cm thick; it is a single homogeneous flow deposit composed of small clasts

(~3–10 cm) that prevail over the fines-rich matrix (Fig. 5A, B). The clast components consist of slightly rounded clasts of the black vesiculated andesite and angular clasts of the gray dense andesite.

The 1 Feb PDC deposits were deposited upon the more widely distributed 14 July PDC deposits. Its PDCs descended the JG and A ravines, as well as six other smaller drainages (Fig. 1C). They left widespread but thin deposits (~1 m) on flat slopes, but form thicker wall-to-wall deposits in narrow ravines. Similar to the 14 July PDC deposits, these are segregated into a poorly-developed top layer of clasts and a fines-rich lower layer, best observed in both the lower JG and A ravines (Fig. 3F).

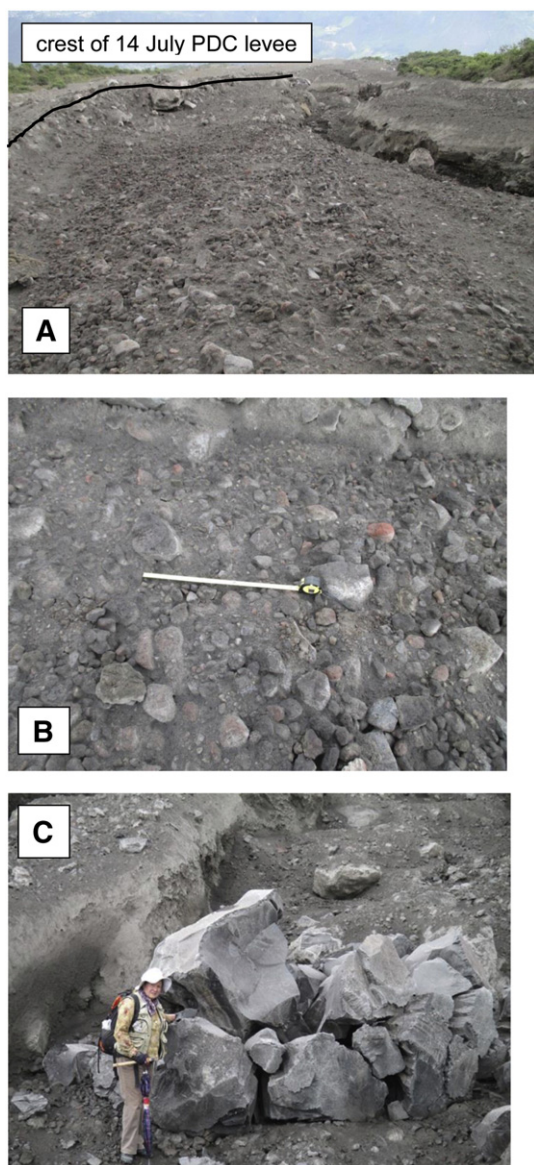


Fig. 5. A & B – The 18 October PDC terminated here near the Cusua Step. It was recognized by being inside the coarse-clast levees of the 14 July PDC, by its homogeneous, small clast-rich deposit only 30 cm-thick, and by its absence in earlier photos. The deposit is not well-compacted and has a large percentage of light gray dense clasts but few black vesicular clasts or accidental fragments. Clasts are both sub-rounded and sub-angular. Tape measure is 50 cm long. C – A 3 m-wide self-fractured bomb of the 18 Oct eruption composed of the dense non-vesicular andesite with an entirely chilled perimeter, that had rolled ~300 m downslope from (Fig. A) location.

The top layer is made up of both sub-angular to sub-rounded clasts of black vesiculated andesite whose diameters rarely exceed 20 cm (Fig. 8B, C), as well as a subordinate number of gray dense andesite clasts. The matrix-rich lower layer carries $\leq 20\%$ clasts whose diameters generally vary between 1 and 10 cm (Fig. 3F). Here clasts of the black vesicular andesite are observed, but the gray dense andesite whose angular clasts have micro-fractures and chilled margins prevails.

6. PDC velocities

Velocities of several 1 Feb PDCs were estimated from video camera registry (Table 2). A mounted video camcorder at OVT (15 km distant) functioned well and the clear weather collaborated to provide an 8 min registry of several PDCs that descended the N to W flanks of the cone. Time was controlled by the camera's chronometer (hr:mm:sec)

and known topographic features on the cone were employed to estimate distances traveled by the flows. Because the clast-rich PDCs are not directly visible, the advance of the visible PDC ash surges were employed to calculate velocities. This calculation does not take into account the time delay between the eruption onset and the initiation of the PDCs, thought to be approx. 10 s: as such, the true velocities will be somewhat faster than those given here. Video registry was not obtained for the 14 July and 18 Oct events due to cloudy conditions and nightfall.

7. PDC eruption volumes

Estimates of PDC volumes, albeit crude, are of interest for comparative reasons as well as for monitoring sequential events in an eruption cycle. These volumes were estimated along drainage channels where their sizes can be approximated by field studies. The measurements are based upon the lengths (slope distances), widths, and deposit thicknesses, as observed or estimated in both the principal and secondary flow channels; they do not include ejecta left on the volcano's upper flanks. While the deposit's channel lengths are well-documented (4.3–7.3 km), their channel widths vary considerably, and consequently minimum (5 m) and maximum (10–25 m) values are employed in the calculation, reflecting the character of each channel. Equally variable, an average deposit's thickness must also be approximated; the value employed varies from 1 to 5 m. Given these conditions the estimate of the total average volume of the PDC deposits of the 14 July 2013 eruption is 1,730,000 m³ and that of the 1 February 2014 eruption is 1,220,000 m³.

Estimates of the total eruption volumes of the 14 July and 1 Feb eruptions were attempted by employing thermal images of the volcano's flanks. A survey of the areas covered by incandescent ejecta for both events was carried out, following a technique of Vallejo et al. (2012). The caveat with this method is that the thermal camera is 15 km from Tungurahua and cannot view the lower slopes and ravines or other sides of the strato-cone. Never-the-less its view encompasses much of the western flanks of the volcano. Based on this imagery, the observable area of incandescent debris was measured, and subsequent field work verified the deposit's distribution and thicknesses for representative sectors. Given these conditions the total emission volumes for the 14 July and 1 Feb eruption are estimated to be 2,780,000 m³ and 5,720,000 m³. Future eruptions will be important to further compare these methods and their respective volumes.

8. Granulometry of the matrix-rich layer of the PDC deposits

Both the 14 July and 1 Feb PDC deposits typically consist of a thicker lower matrix-rich layer and a thinner upper clast-rich layer, as explained in the PDC deposits: morphology and contents section. A granulometric description of the matrix-rich layer is presented here. Because the upper layer contains principally rounded abraded clasts of the juvenile andesites, from -6ϕ to -8ϕ in size and with little fines, it was not analyzed in greater detail.

Samples of the matrix-rich main body of these two PDC deposits were studied in order to determine variation in grain size within the main body and with distance (Fig. 9). Sample fractions were collected from a top level at ~50 cm and from a mid-level at ~250 cm below the clast-rich surface deposit, as well as at random distances (m) from the crater in both the JG-PU and A ravines. Grain-size analyses were performed by mechanical sieving from -6 to $>4\phi$ (64 to <0.063 mm) in full ϕ -steps on these samples. For details see Supplementary material – Granulometry table.

Graphical statistics using the program SFT (Wohletz et al., 1989) show no evidence to distinguish these two eruptions by comparing either their Graphic Mean ($M_z - 0.5$ to 2.33ϕ) or their sorting coefficients (Sigma-I 2.96 to 3.44ϕ , i.e. very poor). A systematic upward coarsening of particle size from the mid-level layer (ave. $M_z - 1.16\phi$)

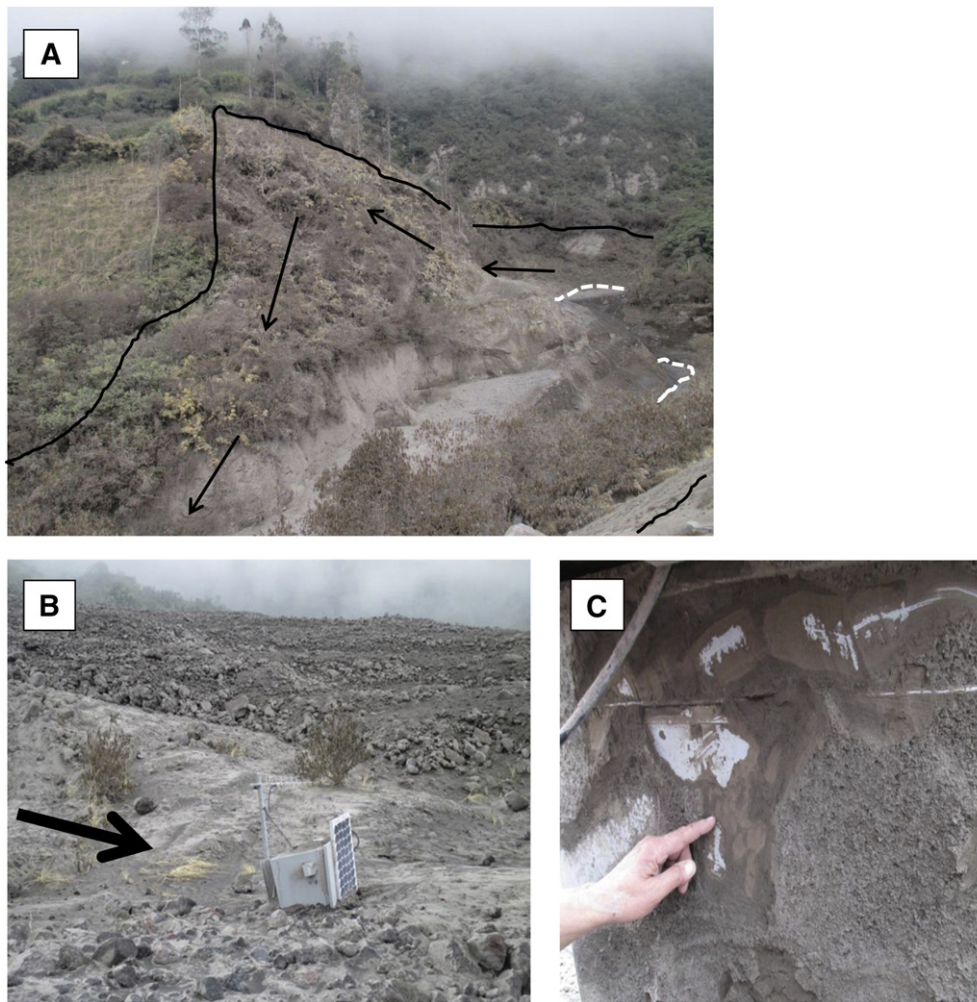


Fig. 6. A – Unlike the 14 July PDC, the 1 Feb PDC was slightly hotter, as witnessed by the wilted, dead, but not burnt vegetation along the lower Juive Grande ravine. The dashed lines mark the PDC deposits at the bottom of the ravine, while the black lines delimit the heat-affected vegetation. Note the effects of the ascent and flow of the heat wave on this tight curve of the channel. B – The 1 Feb PDC-surge impacted this AFM instrument box 5.9 km from the crater and flipped it onto its side. The arrow indicates the surge's flow direction. See details in the text. The 14 July granular PDC flow is seen in the distance. C – The vertical windward side of the AFM box, painted whitish-gray, first records a reddish fine-sandy layer, subsequently overlain by silt-sized black ash, both having been plastered onto the box in the 14 July eruption. During the 1 Feb event the thicker layer of gray gritty ash was plastered onto the box prior to the box being knocked over.

to the upper layer of the matrix-rich layer (ave. $M_z - 1.75 \phi$) is evident in both the 14 July and 1 Feb PDC deposits, when representing the lapilli/ash/extremely fine ash abundance. However, the extremely fine ash ($>4 \phi$) component decreases from 4.75 wt.% on average in the lower level to 1.6 wt.% in its top layer, while the lapilli (-6 to -1ϕ) fraction increases from 48.43 wt.% to 54.28 wt.% (Fig. 9), which supports the inference that elutriation of the finest fraction was important.

9. Effects of PDC heat and the role of water

The effects of PDC heat upon the vegetation were slightly different in the 14 July and 1 Feb eruptions. Leafy brush only 2–5 m above the 14 July PDC deposits at 6.9 km distance was only wilted, but subsequently died. In comparison, the 1 Feb PDC at the same site and channel left notable bands of progressively less wilted, but unburnt dead vegetation, from the base of the channel upwards. These bands varied in color from yellow-tan near the base (≤ 10 m) to gray-tan at intermediate heights (~ 20 m), to normal green coloration at ~ 30 m above the warm PDC deposits (Fig. 6A). A temperature of 171°C was registered

in the 1 Feb PDC deposits at 70 cm depth eight days after the event (B. Bernard, pers. com., 2014).

Nowhere did the brush ever attain a combustion temperature, estimated to be in the ~ 250 – 300°C range for this environment (Babrauskas, 2001). Nevertheless, plastic-coated electrical wiring in close proximity to the 1 Feb PDC deposits did melt, suggesting a temperature range of 100 – 250°C . Charred or carbonized wood was rarely found associated with these PDC deposits. Ten hours after the 14 July eruption, most small clasts (~ 10 cm diameters) on the surface of the JG-PU PDC deposit, 6.6 km from the crater, were still very warm, however large dense blocks (≤ 1 m size) were too hot to touch. Similar low temperatures of 100 – 300°C were reported at Merapi (Boudon et al., 1993; Jenkins et al., 2013), as well as at Soufriere Hills (Cole et al., 2002), but such measurements were often made near the PDC's termination. At Tungurahua as elsewhere (Cole et al., 2002), the PDC's apparent low temperatures are thought to be due to cooling caused by the large distance traveled and the degree of air entrainment, favored here by their descent down Tungurahua's steep, stepped terrain.

The important role of water in eruptions is well known, but meteoric water appears to have played only a minor role in the formation and

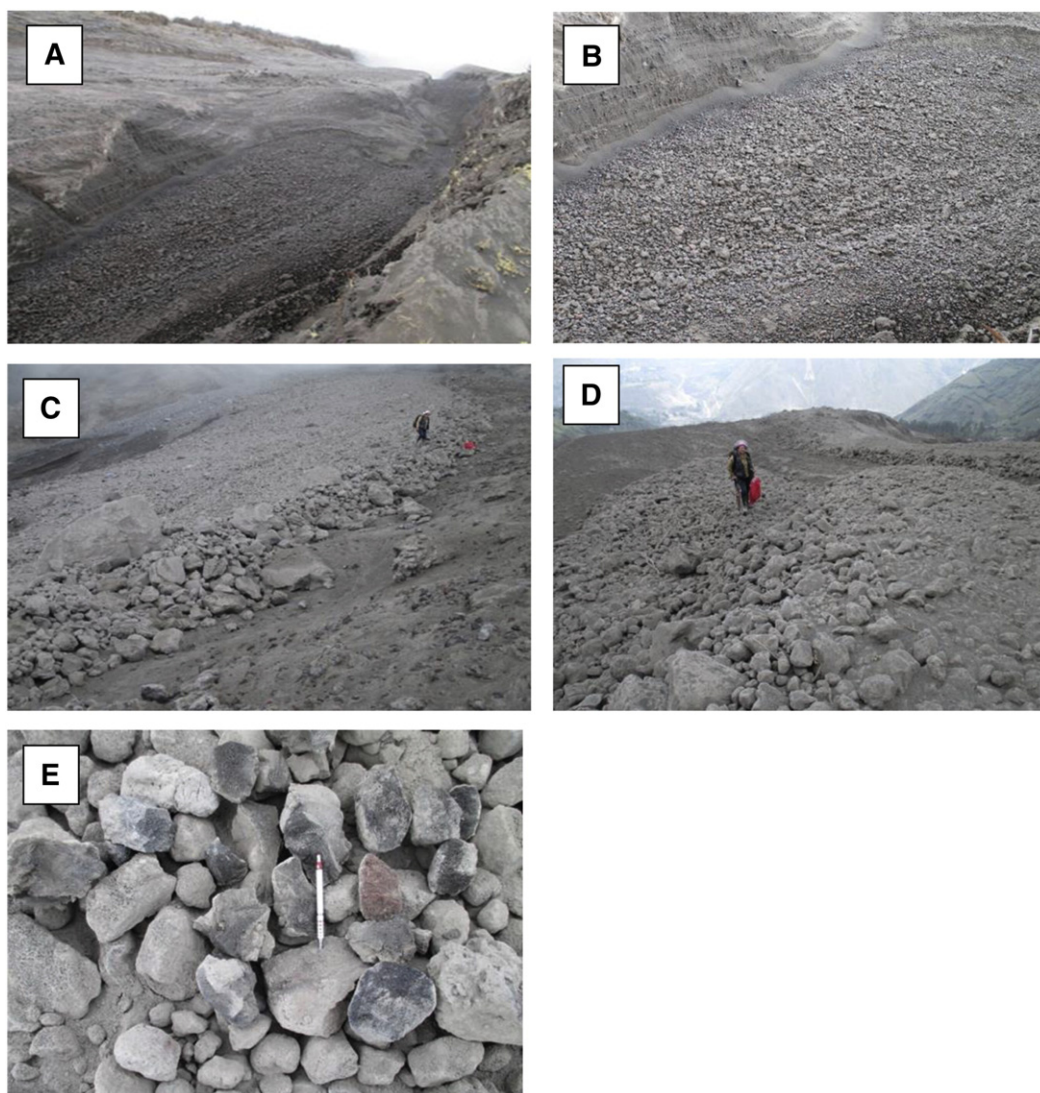


Fig. 7. A & B – The 1 Feb PDC deposit in JG ravine at 4.4 km from the crater. The 40 m-wide flow backed up on this topographic step before descending more steeply. Note the linear trains of both large and small clasts, the largest blocks being 3–5 m across. The trains would suggest internal segregation as well as varying velocities. C – Here at 5.9 km from the crater, the 1 Feb PDC spread out upon a topographic step in the JG ravine. The PDC lobes have widths ≤ 30 m and formed well-developed levees with large clasts. The clast-rich surface layer is underlain by a 1 m-thick matrix-rich layer, such as seen in Fig. 3F. Photo taken on 8 Feb. 2014. D – Two overlapping snouts of the 14 July PDCs, both of which have convex profiles without levees. These contrast sharply with the 1 Feb PDC lobes seen in the distance and in (C) which have planar non-convex morphologies with notable levees. The difference in their morphology is likely due to the thickness of their fines-rich interior. E – The dominant clasts of the 1 Feb PDC deposit seen here are all partially rounded, well-vesiculated black andesites, with abraded perimeters coated on all sides by white powder, the likely dusty product of clast–clast abrasion.

behavior of these PDC flows and their deposits. There is an almost permanent absence of water in the ravines, and there was insignificant rainfall in the hours prior to these eruptions. Furthermore the floors of these ravines were vegetation- and soil-free and consequently could have supplied little moisture. Corroborating this assessment is the fact that no steam was observed escaping from the 14 July deposits 10 h after the eruption in either the JG–PU or A channels.

10. PDC-surge and elutriated ash cloud deposits

Fine-grained dilute pyroclastic flows accompanied the block-and-ash PDCs and left their deposits as coatings upon the lower slopes of the volcano. We distinguish PDC-surges as dilute flows whose velocity, direction, and dynamic force seem to be associated with the PDC itself. These surges left millimeter-thick layers of poorly sorted silt- and sand-sized particles plastered or caked upon vertical posts, trees, and instrument boxes, up to a height of several meters, corroborating that they were fast, quasi-horizontal flows. One surge had sufficient energy to flip over a heavy metal instrument box (see below). The PDC-surge

deposits were readily distinguished, as they tend to coat or plaster vertical surfaces, encountered along their path (Fig. 6C).

In addition we recognize a fine-grained ash that was observed being lofted several hundred meters above the descending PDC; apparently this ash had been elutriated from the PDCs as they descended the volcano's steep irregular topography. Subsequently this ash settled out of the air by gravity and covered the top surface of the landscape with centimeter-thick layers of well-sorted, loose, fine ash, often near the routes followed by its PDC.

In their study of the ash deposits of Tungurahua's 2006 eruption, Eychenne et al. (2011) recognized two distinct size populations and concluded that plume-derived ash falls contained ash particles generally greater than 0.25 mm in size, while PDC-surge particles were generally less than 0.063 mm. In the present study, ash samples, each totaling 15 to 20 liters, were collected from a variety of sites; they were sieved on site using a 0.25 mm sieve to roughly determine their relative unpacked volumes. PDC ash cloud deposits that blanketed the 14 July PDC deposits at two JG ravine sites consisted of at least 83 vol.% and 100 vol.% of fine particles less than 0.25 mm in size. Away from the

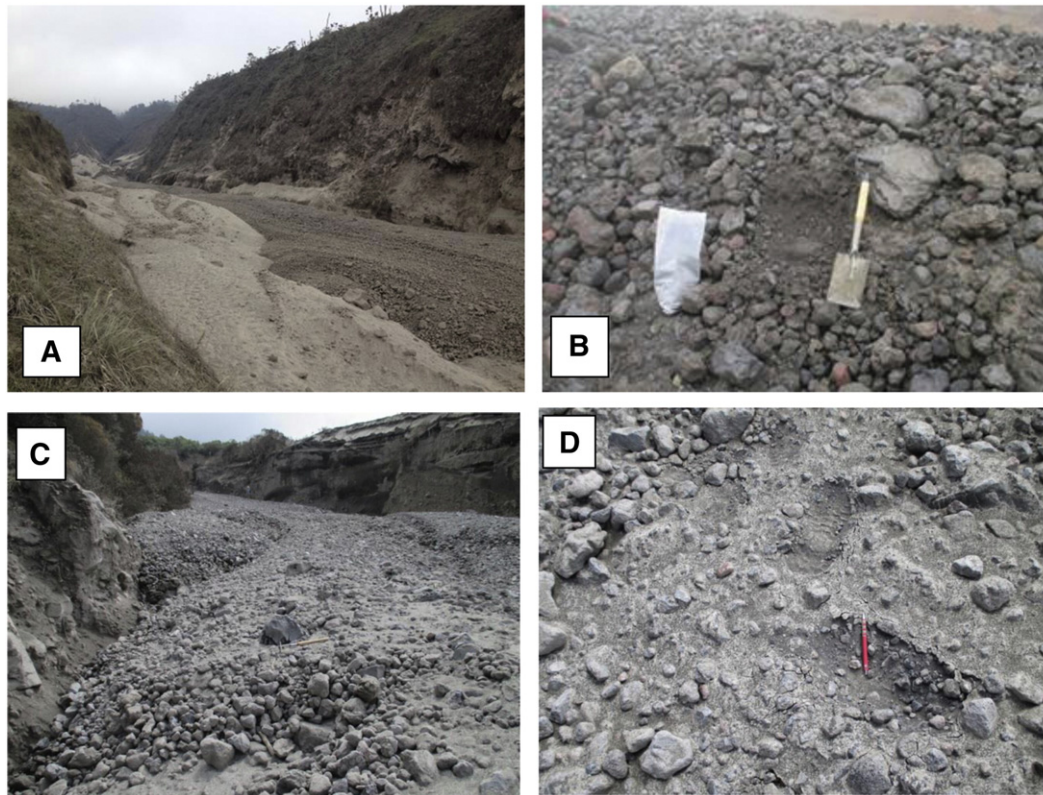


Fig. 8. A – The 1 Feb PDC deposits, approximately 20 m-wide, in the lower Achupashal ravine near the flow's termination. Remnants of the 14 July PDC deposit underlie a bench in the foreground. B – The clast-rich levee of the 1 Feb PDC deposit and its fines-rich interior. C & D – Lobes of the 1 Feb PDC as seen in the lower JG ravine 6.6 km from the crater. Note the composite series of lobes, the youngest pulse by-passing slightly older pulses. Again the lobes have convex cross-sections with clast-rich margins and leading edges, while a fine-grained matrix dominates the central surface axis of the same lobe (D). The 1 Feb PDC bed is ~1 m-thick (see Fig. 3D). Note the umbrella and pencil for scale in C and D, respectively.

JG–PU valley and its PDC deposits and using the same technique, ash layers thought to be plume-derived contained at least 54 vol.% of material ≥ 0.25 mm in size and 46 vol.% ≤ 0.25 mm. These tentative results generally agree with those of Eychenne.

Along the JG–PU ravine, the 14 July PDC veered sharply northward near the AFM stations and followed the main ravine, but its accompanying PDC-surge decoupled and continued onward down the JG fan where it left a thin powdery covering. Little of this surge's ash descended the main JG ravine (Fig. 3B, C). In A ravine however, the 14 July PDC-surge followed the deep narrow ravine, where it was greatly constrained by the 20–30 m high vertical sides of the canyon (Fig. 4A). The higher parts of the surge surpassed the canyon's walls and left a thin ash coating upon the adjacent interfluvies (Fig. 4E). Where it crossed the Baños–Bilbao highway, this PDC-surge left an ~10 cm-thick layer of gray, hot, fluidized ash that laid directly upon the 14 July block-and-ash PDC deposit. It consists of at least 77 vol.% of the ≤ 0.25 mm fraction. In order to document the possible contribution of fine ash from the main PDC deposit, its top-most matrix fraction was sieved and consisted of 55 vol.%

of the ≤ 0.25 mm ash and 45 vol.% of the ≥ 0.25 mm ash. As such, this upper matrix fraction would have been a likely source of fine particles.

The 1 Feb PDC followed the same JG–PU path as that of the 14 July PDC. Upon reaching the flat area near the AFM stations, the clast-rich PDC again turned to the north and followed the main JG ravine. Some PDC-surges accompanied the PDC and left thin ash coatings up to 700 m farther down the JG ravine. However, near the stations a PDC lobe continued straight down the fan, accompanied by its surge, which left a thin powdery covering upon the lobe and the central fan.

Fine ash of the 1 Feb PDC-surge that had been plastered against antenna posts and an instrument box next to the JG ravine was also studied. A vertical post located in the lower JG valley was coated with a 3–5 mm-thick layer composed of 97 vol.% fine gray ash whose particles are ≤ 0.50 mm in size. The metal AFM box located at 5.9 km from the crater and ~30 m from the nearest PDC lobe at a mid-level site (2390 m elev.) was coated on its up-valley side by two very fine layers of compacted ash (Fig. 6B, C). The inner older layer had slightly coarser

Table 2
Estimated PDC velocities.

1 Feb PDC velocity based upon video imagery	Slope distance traveled	Travel time from eruption onset	Velocity (approx.)
Romero Ravine	~1660 m	175 s	Minimum 9.5 m/s
Hacienda Ravine	~5510 m	465 s	11.8 m/s
Vascún Ridge	~2170 m	65 s ^a	33 m/s (M. Hall)
Vascún Ridge Thermal Imagery	Approx. 2000 m		36 m/s (S. Vallejo)
Achupashal Ravine (PDC surge)	~4750 m	273 s	17.4 m/s
Achupashal Ravine (registered by OVT camera)	~5620 m	411 s	13.7 m/s (distance poorly controlled)
Achupashal Ravine – as PDC terminated	Last ~337 m of path	41 s	8.2 m/s
Crater to AFM stations along JG path observed by thermal camera at OVT	~5900 m	333 s	17.7 m/s (an overall estimate)

^a Travel time observed from the 1st sighting of descending flow to the flow's arrival at recognized topographic feature. The higher velocities reported for Vascún Ridge may be due to a directed-blast onset, given that its surge cloud left the crater area with greater velocity than other PDCs which appeared to be of fountain collapse origin.

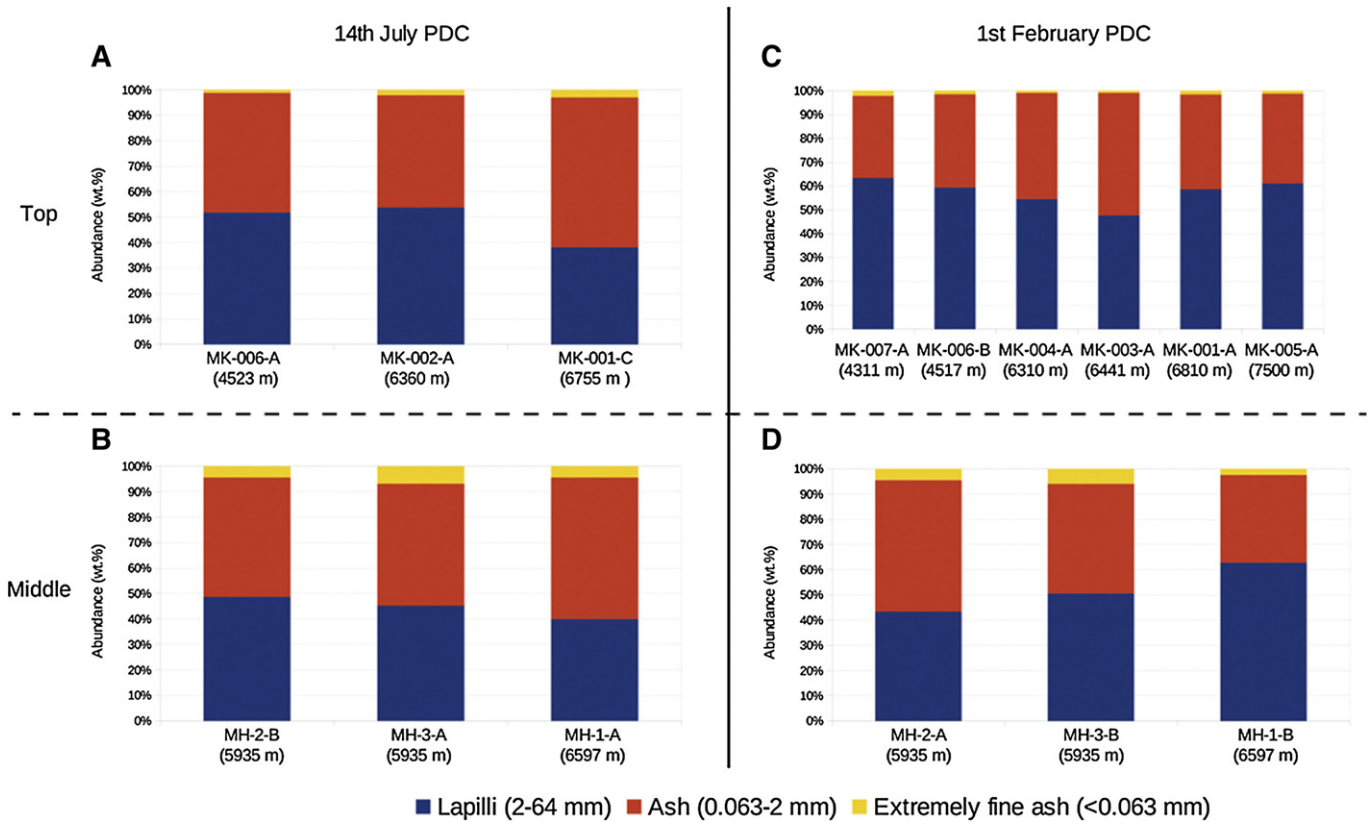


Fig. 9. Abundance (wt.%) histograms for the lapilli (-6 to -1ϕ)/ash (-1 to 4ϕ)/extremely fine ash ($>4\phi$) fractions from the 14 July 2013 to 1 Feb 2014 PDC samples. Each histogram sample is arranged according to the slope distance (m) traveled from crater (proximal to the left and distal to the right). Samples from the dominant matrix-rich part of the PDC deposits are designated “top” (the uppermost fraction) and “middle” (a mid-section fraction). See Section 8 of the text.

particles (77 vol.% of ≤ 0.25 mm size fraction) and its reddish color suggested that its source was the 14 July eruption. The ash of the outer gray layer (90 vol.% of ≤ 0.25 mm size) corresponds to the recently deposited 1 Feb PDC-surge.

This same AFM box was impacted and flipped onto its adjacent downwind side by the 1 Feb PDC-surge. The impacted side of the box was caked with a millimeter-thick layer of the outer gray ash of the 1 Feb PDC-surge, also seen on nearby antenna posts and boulders. Since the ash layer occurs only on what had been the upwind side of the box, it is apparent that the box was flipped by this surge event. Here we attempt to estimate the necessary dynamic pressure of the surge required to overturn this box. The impacted side of the metal box has an area of 4801 cm², a height of 57 cm, and a total mass of ~ 60 kg, comprised of the box, two large car batteries, and electronic equipment. The box was set in soil by means of two short steel rods. The minimum dynamic pressure of the PDC-surge required to flip the box is estimated at ~ 1.2 kPa scales. Similar values were reported at Merapi by Jenkins et al. (2013) who calculated that the felling of slim trees and bamboo required dynamic pressures of 1–2 kPa while poorly reinforced concrete frame masonry failed at around 2–4 kPa.

11. Discussion and results

Well-monitored by a 5-station broadband seismic and acoustic array, the 2013–2014 Tungurahua eruptions were some of the most energetic and intense Vulcanian eruptions ever recorded anywhere, although each lasted only 10–20 min. Notably, no correlation seems to exist between the magnitude of the eruptions and the prospect of the generation of large PDCs, as observed by comparing eruptions of the past 8 years. Such an unexpected relation might be due to a lesser volume of material (juvenile magma, plug rocks, older conduit material)

available to be ejected to form PDCs, and apparently not to low explosive energy.

From 2006 to 2010 Tungurahua's eruptive activity reached intense Strombolian to Sub-Pinian levels (Hall et al., 2013). However, in the eruptions from 21 August 2012 to 1 February 2014, the activity continued to increase, reaching intense Vulcanian levels. During this same period, it was noted that the repose intervals between eruptions were 3.5-, 7-, 3-, and 3.5-months long, leading us to infer sequential pressurization cycles that end with highly energetic explosions. This cyclic behavior suggests that the preceding magmas that remained in the uppermost conduit underwent crystallization and solidification, resulting in a blockage or plugging of the conduit, while the magma of the lower part of the conduit experienced pressurization of its gas content. Favoring this interpretation, the eruption with the largest acoustic energy release of this series followed the longer 7 month repose interval. This cyclic pattern was also registered by both tiltmeter and GPS monitoring high up on the cone (P. Mothes, pers. comm., 2014).

That the ascending juvenile magma came in contact with the plug somewhere in the magma conduit is seen in Fig. 10, where foamy gas-rich magma has intruded a set of parallel fractures, thought to be older, in the core of the block. However, the dense plug rock of the block's exterior has wedge-shaped expansion fractures, apparently the result of post-decompression or post-eruption cooling. The highly vesiculated scoria clasts of the PDC's cauliflower blocks are the likely remnants of this top-most magma. With the explosive fragmentation of the plug, a multitude of fragments and particles were ejected and became widely dispersed over the upper slopes of the cone. These plug fragments (dense microcrystalline andesite) along with pieces of the juvenile magma (well-vesiculated aphyric andesite) and incorporated accidental blocks together form the materials of the PDC flows. Decompression events may have been at depths of ~ 1.5 km (Kim

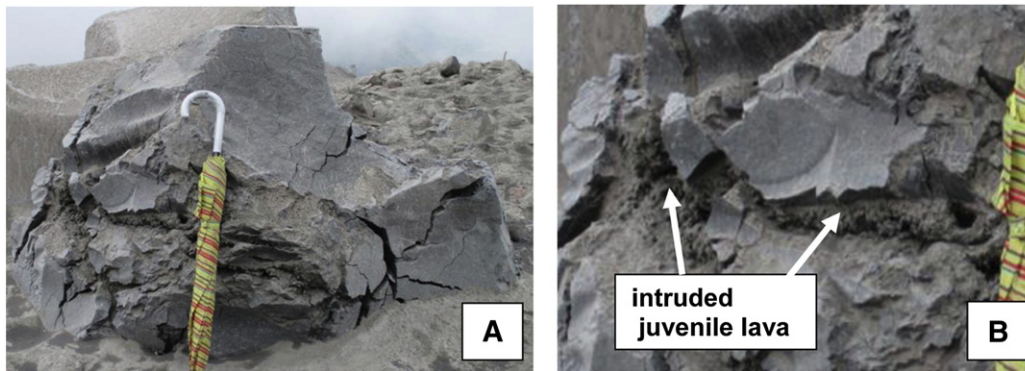


Fig. 10. A & B – Large blocks of gray non-vesicular dense andesite of 14 July, a remnant of the presumed conduit plug. The block's core developed parallel fractures which were then intruded by gas-rich juvenile lava, implying that this rock was near the interface of the plug and the top of the magma column. Subsequently the plug rock was ejected during decompression, resulting in its cooling and the formation of large expansion fractures on the block's exterior.

et al., 2014) or ~6 km (Kumagai et al., 2011), based upon registered hypocenter seismic events.

The 1 February eruption generated medium-size PDCs, chiefly by fountain collapses and a small lateral blast, as interpreted from video images. The short but intense Vulcanian eruptions of 2013–2014 resulted in small PDC volumes, as compared to the PDCs of the 16 August 2006 eruption, which witnessed ~6 h of continuous, powerful Strombolian to Sub-Plinian activity that produced many pyroclastic flows of varying sizes with a total volume of $\sim 27 \times 10^6 \text{ m}^3$ of ejecta. A Vulcanian-level of activity could not be verified for that eruption. The total erupted volumes of the 14 July 2013 and the 1 February 2014 eruptions are estimated at 2.8 and $5.7 \times 10^6 \text{ m}^3$, respectively.

Block-and-ash PDCs descended the N, NW, and W flanks of Tungurahua upon 27° to 14° slopes for distances of 5–7 km with a total vertical drop of up to 2.8 km. The velocities of the 1 Feb PDCs varied between 11 and 18 m/s, in addition to a lateral blast of ~33 m/s. The mobility and distance traveled by the PDCs appear to be related to the volume of fines available from the explosion and fountain collapses, as well as that generated by clast–clast abrasion during transport. Furthermore, mobility was probably enhanced by air entrainment during PDC descent, favored by the exceptionally steep, stepped topography, which is corroborated by the very fluidized ash deposits seen on the 14 July PDC lobes. Being confined laterally within narrow ravines also favored PDC mobility. In addition, the upward segregation of coarser clasts within the PDCs enriched its lower layer in fines, as observed, likely increasing the PDC's mobility, as well as the piggy-back transport of less dense juvenile andesite clasts toward the top of the PDC flows.

Upon gradual or flat slopes, the larger PDCs display tongue-shaped flow deposits with levees, but in narrow restricted ravines the PDCs simulate a series of consecutive lobate pulses each with a convex profile and with few levees. In the lower reaches, PDC lobes are often made up of two layers: (1) a thinner upper layer dominated by rounded, abraded clasts with little intra-clast matrix, the clasts being composed chiefly of the well-vesiculated juvenile andesite and (2) a thicker lower layer dominated by sand- and silt-sized fines and with few angular clasts ≥ 5 cm in size. The upper layer is apparently the result of clast segregation, in which larger less-dense clasts migrated to the flow's surface, leaving a thicker fines-rich reversely-graded lower layer. In the July and February eruptions PDC-surges and elutriated ash clouds left thin mantles of fine ash upon the volcano's flanks.

The recent eruption cycles of Tungurahua volcano have each ended with small lava flows composed of poorly vesiculated magma. This magma was left in the upper conduit where it further de-gassed and slowly formed a sealed plug of poorly crystallized andesite. Gas pressurization of the lower conduit ensued, as a result of the gradual but continued ascent of magmatic gases. However, after 3–4 months the plug failed, abrupt decompression followed, and the plug was blown apart, as attested to by the very high acoustic energies. The eruption cycle

repeats itself as the conduit again becomes sealed by the eventual solidification of new juvenile magma. Similar scenarios were reported by Wright et al. (2007) at Guagua Pichincha volcano, but there, shallow conduit blockage was achieved by dome formation and growth, reported also by Burgisser et al. (2011) for the pre-explosive conduit conditions at Soufrière Hills volcano.

The character of the recent eruptions of Tungurahua carries a social burden, given the intensity of the explosions, the abrupt eruption onsets without much warning, the lengthy, rapid PDCs that can easily reach villages and the principal highway. Baños located at the foot of the volcano and with a population of more than 20 k has not been directly affected so far by PDCs or lavas. Fortunately the status of the monitoring instrumentation and the Institute's experience gained from closely observing the volcano during more than 15 years, as well as the good constant dialogue between the population and the scientific team will aid in future volcanic crises.

Supplementary data to this article can be found online at <http://dx.doi.org/10.1016/j.jvolgeores.2015.09.009>.

Acknowledgments

The authors would like to acknowledge the momentous efforts of the entire IG staff, especially the electronic and scientific personnel, for the successful monitoring of Tungurahua volcano and the continued evaluation and interpretation of the endless data stream. We honor and thank the Iván Chávez Family of Baños for the continued use of their property which houses the Observatorio Volcanológico de Tungurahua. The sophisticated level of monitoring and data interpretation is due to the help received from H. Kumagai and the Japan International Cooperation Agency (JICA) and the VDAP program of the United States Geological Survey, sponsored by USAID. We also acknowledge the Ecuadorian government's SENACYT and SEMPLADES programs, as well as the Secretario de Gestión de Riesgos for their support, as well as the Escuela Politécnica Nacional and the Institut de Recherche pour le Développement of France. We also thank J. Stone for drone photos, F. Vásquez for help in the field, and E. Gaunt for discussions of the plug rock. We thank M. Ort and D. Geist for constructive reviews.

Appendix A. Explosion amplitude and energy calculations

Seismic amplitudes are expressed as reduced displacement (D_R) in cm^2 and devised by multiplying the root mean square (rms) of the seismic signal by the distance from source to receiver, correcting amplitude data to a common reference point, the vent. A reduced displacement value is derived independently at four broadband stations (BMAS, BPAT, BRUN, and BBIL) and then a single, averaged explosion D_R (D_{R_MEAN} ; Table 1) is computed by taking the mean amplitude between the station's values.

For acoustic signals, calculated peak-to-peak amplitudes are normalized to a distance of 1 km from the vent and expressed as reduced pressure (P_R) in Pascals (Pa). This is achieved under the assumption that excess pressure amplitude decays as the inverse of propagation distance $1/r$, where r is the distance from the vent to the monitoring instrument (Johnson and Ripepe, 2011; Fee and Matoza, 2013). An averaged P_R value (P_{R_MEAN} ; Table 1) is obtained by taking the mean reduced pressure between four infrasound sensors that are collocated to the seismic stations.

Time integrated explosion energies are approximated across the entire seismic and acoustic transients and expressed in Joules (J). Acoustic energy (E_A) radiated into the atmosphere during a discrete impulsive exhalation is estimated through space–time integration over a hemispherical surface, by assuming isotropic radiation of a linear elastic wave propagating through a homogeneous atmosphere, while seismic energy (E_S) is considered proportional to the product of the volcano density and the squared particle velocity integrated over the volcano volume (see Johnson and Aster, 2005). An averaged seismic and acoustic energy value (E_{S_MEAN} and E_{A_MEAN} , respectively; Table 1) are calculated by taking the mean radiated energy between the four monitoring sites mentioned above, in a similar fashion to calculations of averaged amplitude measurements. Before analysis, seismic signals are band-pass filtered between 0.5 and 12 Hz and acoustic signals between 0.1 and 25 Hz.

References

- Babrauskas, V., 2001. Ignition of wood: a review of the state of the art. *Interflam*. Interscience Communications Ltd., London, pp. 71–88.
- Bernard, B., Hidalgo, S., Robin, C., Beate, B., Quijocaza, J., 2014. The 3640–3510 BC rhyodacite eruption of Chachimbiro compound volcano, Ecuador: a violent directed blast produced by a satellite dome. *Bull. Volcanol.* 76, 1–20. <http://dx.doi.org/10.1007/s00445-014-0849-z>.
- Boudon, G., Camus, G., Gourgaud, A., Lajoie, J., 1993. The 1984 nuée-ardente deposits of Merapi volcano, Central Java, Indonesia: stratigraphy, textural characteristics, and transport mechanisms. *Bull. Volcanol.* 55, 327–342.
- Burgisser, A., Arbaret, L., Druitt, T., Giachetti, T., 2011. Pre-explosive conduit conditions of the 1977 Vulcanian explosions at Soufrière Hills Volcano, Montserrat: II. Overpressure and depth distributions. *J. Volcanol. Geotherm. Res.* 199, 193–205.
- Charbonnier, S.J., Germa, A., Connor, C.B., Gertisser, R., Preece, K., Komorowski, J.-C., Lavigne, F., Dixon, T., Connor, L., 2013. Evaluation of the impact of the 2010 pyroclastic density currents at Merapi volcano from high-resolution satellite imagery, field investigations and numerical simulations. *J. Volcanol. Geotherm. Res.* 261, 295–315. <http://dx.doi.org/10.1016/j.jvolgeores.2012.12.021>.
- Cole, P.D., Calder, E.S., Sparks, R.S.J., Clarke, A.B., Druitt, T.H., Young, S.R., Herd, R.A., Harford, C.L., Norton, G.E., 2002. Deposits from dome-collapse and fountain-collapse pyroclastic flows at Soufrière Hills Volcano, Montserrat. In: Druitt, T.H., Kokelaar, B.P. (Eds.), *The Eruption of Soufrière Hills Volcano, Montserrat, From 1995 to 1999*. Geological Society of London, Memoirs 21, pp. 231–262.
- Cronin, S.J., Lube, G., Dayudi, D.S., Sumarti, S., Subrandiyo, S., Surono, 2013. Insights into the October–November 2010 Gunung Merapi eruption (Central Java, Indonesia) from the stratigraphy, volume and characteristics of its pyroclastic deposits. *J. Volcanol. Geotherm. Res.* 261, 244–259.
- Douillet, G.A., Tsang-Hin-Sun, E., Kueppers, U., Letort, J., Pacheco, D., Goldstein, F., Von Aulock, F., Lavallée, Y., Hanson, J.B., Bustillos, J., Robin, C., Ramón, P., Hall, M., Dingwell, D., 2013. Sedimentology and geomorphology of the deposits from the August 2006 pyroclastic density currents at Tungurahua volcano, Ecuador. *Bull. Volcanol.* 75, 765–786.
- Druitt, T.H., Young, S.R., Baptie, B., Bonnadona, C., Calder, E.S., Clarke, A.B., Cole, P.D., Harford, C.L., Herd, R.A., Lockett, R., Ryan, G., Voight, B., 2002. Episodes of cyclic Vulcanian explosive activity with fountain collapse at Soufrière Hills Volcano, Montserrat. In: Druitt, T.H., Kokelaar, B.P. (Eds.), *The Eruption of Soufrière Hills Volcano, Montserrat, From 1995 to 1999*. Geological Society of London, Memoirs 21, pp. 281–306.
- Eychenne, J., Le Pennec, J.-L., Troncoso, L., Gouhier, M., Nedelec, J., 2011. Causes and consequences of bimodal grain-size distribution of tephra fall deposited during the August 2006 Tungurahua eruption (Ecuador). *Bull. Volcanol.* <http://dx.doi.org/10.1007/s00445-011-0705-17>.
- Fee, D., Matoza, R.S., 2013. An overview of volcano infrasound: from Hawaiian to Plinian, local to global. *J. Volcanol. Geotherm. Res.* 249, 123–139.
- Freundt, A., Wilson, C.J., Carey, S.N., 2000. Ignimbrites and block-and-ash flow deposits. In: Sigurdsson, et al. (Eds.), *Encyclopedia of Volcanoes*, Academic Press, pp. 581–600.
- Hall, M., Robin, C., Beate, B., Mothes, P., Monzier, M., 1999. Tungurahua volcano, Ecuador: structure, eruptive history and hazards. *J. Volcanol. Geotherm. Res.* 91, 1–21.
- Hall, M., Steele, A., Mothes, P., Ruiz, M., 2013. Pyroclastic density currents (PDC) of the 16–17 August 2006 eruptions of Tungurahua volcano, Ecuador: geophysical registry and characteristics. *J. Volcanol. Geotherm. Res.* 265, 78–93.
- Hildreth, W., Fierstein, J., 2012. The Novarupta–Katmai eruption of 1912 – largest eruption of the 20th century. *US Geol. Surv. Prof. Pap.* 1791 (259 pp.).
- Iverson, R.M., Vallance, J.W., 2001. New views of granular mass flows. *Geology* 29 (2), 115–118. [http://dx.doi.org/10.1130/0091-7613\(2001\)029-0115:VOGMF>2.0.CO;2](http://dx.doi.org/10.1130/0091-7613(2001)029-0115:VOGMF>2.0.CO;2).
- Jenkins, S., Komorowski, J.-C., Baxter, P.J., Spence, R., Picquout, A., Lavigne, F., Surono, 2013. The Merapi 2010 eruption: an interdisciplinary impact assessment methodology for studying pyroclastic density dynamics. *J. Volcanol. Geotherm. Res.* 261, 316–329.
- Johnson, J.B., Aster, R.C., 2005. Relative partitioning of acoustic and seismic energy during Strombolian eruptions. *J. Volcanol. Geotherm. Res.* 148, 334–354.
- Johnson, J.B., Ripepe, M., 2011. Volcano infrasound: a review. *J. Volcanol. Geotherm. Res.* 206 (3–4), 61–69.
- Johnson, C.G., Kokelaar, B.P., Iverson, R.M., Logan, M., LaHusen, R.G., Gray, J.M., 2012. Grain-size segregation and levee formation in geophysical mass flows. *J. Geophys. Res.* 117. <http://dx.doi.org/10.1029/2011JF002185>.
- Kelfoun, K., Samaniego, P., Palacios, P., Barba, D., 2009. Testing the suitability of frictional behavior for pyroclastic flow simulation by comparison with a well-constrained eruption at Tungurahua volcano (Ecuador). *Bull. Volcanol.* <http://dx.doi.org/10.1007/s00445-009>.
- Kim, K., Lees, J., Ruiz, M., 2014. Source mechanism of Vulcanian eruption at Tungurahua volcano, Ecuador, derived from seismic moment tensor inversions. *J. Geophys. Res.* <http://dx.doi.org/10.1002/2013JB010590>.
- Komorowski, J.-C., Jenkins, S., Baxter, P.J., Picquout, A., Lavigne, F., Charbonnier, S., Gertisser, R., Preece, K., Cholik, N., Budi-Santosa, A., Surono, 2013. Paroxysmal dome explosion during the Merapi 2010 eruption: processes and facies relationships of associated high-energy pyroclastic density currents. *J. Volcanol. Geotherm. Res.* 261, 260–294. <http://dx.doi.org/10.1016/j.jvolgeores.2013.01.007>.
- Kumagai, H., Palacios, P., Ruiz, M., Yepes, H., Kozono, T., 2011. Ascending seismic source during an explosive eruption at Tungurahua volcano, Ecuador. *Geophys. Res. Lett.* 38, L01306. <http://dx.doi.org/10.1029/2010GL045944>.
- Le Pennec, J.-L., Jaya, D., Samaniego, P., Ramon, P., Moreno, S., Egred, J., Van der Plicht, J., 2008. The AD 1300–1700 eruptive periods at Tungurahua volcano, Ecuador, revealed by historical narratives, stratigraphy and radio carbon dating. *J. Volcanol. Geotherm. Res.* 176, 70–81.
- Loughlin, S.C., Calder, E.S., Clarke, A.B., Cole, P.D., Lockett, R., Mangan, M.T., Pyle, D.M., Sparks, R.S., Voight, B., Watts, R.B., 2002. Pyroclastic flows and surges generated by the 25 June 1997 dome collapse, Soufrière Hills Volcano, Montserrat. In: Druitt, T.H., Kokelaar, B.P. (Eds.), *The Eruption of Soufrière Hills Volcano, Montserrat, From 1995 to 1999*. Geological Society of London, Memoirs 21, pp. 191–210.
- Marchetti, E., Ripepe, M., Harris, A.J.L., Delle Donne, D., 2009. Tracing the differences between Vulcanian and Strombolian explosions using infrasonic and thermal radiation energy. *Earth Planet. Sci. Lett.* 279, 273–281.
- McNutt, S., Tytgat, G., Estes, S., Stihler, S., 2010. A parametric study of the January 2006 explosive eruptions of Augustine volcano, using seismic, infrasonic, and lightning data. In: Power, J.A., Coombs, M.L., Freymueller, J.T. (Eds.), *The 2006 Eruption of Augustine Volcano, Alaska*. USGS Prof. Paper 1769, pp. 85–104.
- Morrissey, M., Chouet, B., 1997. Burst conditions of explosive volcanic eruptions recorded on microbarographs. *Science* 275, 1290–1293.
- OVT Weekly Reports No. 699, 713, 728, 729. Observatorio Volcanológico de Tungurahua. IGEPN, Quito [www.igepn.edu.ec/Volcanoes/Tungurahua/Informes Semanales](http://www.igepn.edu.ec/Volcanoes/Tungurahua/Informes%20Semanales)
- Petersen, E.T., De Angelis, S., Tytgat, G., McNutt, S.R., 2006. Local infrasound observations of large ash explosions at Augustine Volcano, Alaska, during January 11–28, 2006. *Geophys. Res. Lett.* 33, L12303. <http://dx.doi.org/10.1029/2006GL026491>.
- Ritchie, L.J., Cole, P.D., Sparks, R.S.J., 2002. Sedimentology of deposits from the pyroclastic density current of 26 December 1997 at Soufrière Hills Volcano, Montserrat. In: Druitt, T.H., Kokelaar, B.P. (Eds.), *The Eruption of Soufrière Hills Volcano, Montserrat, From 1995 to 1999*. Geological Society of London, Memoirs 21, pp. 435–456.
- Samaniego, P., Le Pennec, J., Robin, C., Hidalgo, S., 2011. Petrological analysis of the pre-eruptive magmatic process prior to the 2006 explosive eruptions at Tungurahua volcano (Ecuador). *J. Volcanol. Geotherm. Res.* 199, 69–84.
- Stix, J., Torres, R., Narváez, L., Cortés, G., Raigosa, J., Gómez, D., Castonguay, R., 1997. A model of Vulcanian eruptions at Galeras volcano, Colombia. *J. Volcanol. Geotherm. Res.* 77, 285–303.
- Vallejo, S., Le Pennec, J.-L., Kelfoun, K., Harris, A., 2012. Calibration of volcanic flow simulations using thermal images: the 4th and 9th December 2010 eruption of Tungurahua volcano (Ecuador): project study. *Laboratoire Magmas et Volcans, Univ. Blaise Pascal, Clermont–Ferrand* (44 pp.).
- Williams, H., 1941. Calderas and their origin. *Univ. Calif. Publ. Geol. Soc.* 25 (6), 239–346.
- Wilson, L., Head, J.W., 1981. Morphology and rheology of pyroclastic flows and their deposits, and guidelines for future observations. In: Lipman, P.W., Moullineux, D.R. (Eds.), *The 1980 Eruptions of Mount St. Helens, Washington*. US Geol Surv Prof Paper 1250, pp. 513–524.
- Wohletz, K.H., Sheridan, M.F., Brown, W.K., 1989. Particle size distributions and the sequential fragmentation/transport theory applied to volcanic ash. *J. Geophys. Res.* 94, 15,703–15,721.
- Wright, H., Cashman, K., Rosi, M., Cioni, R., 2007. Breadcrust bombs as indicators of Vulcanian eruption dynamics at Guagua Pichincha volcano, Ecuador. *Bull. Volcanol.* 69, 281–300.
- Wright, H., Cashman, K., Mothes, P., Hall, M., Ruiz, A.G., Le Pennec, J.-L., 2012. Estimating rates of decompression from textures of erupted ash particles produced by 1999–2006 eruptions of Tungurahua volcano, Ecuador. *Geology* 40, 619–622.